

Composite Molecular Sieve ZSM-5/MCM-48-Based Impregnation Modification for Efficient Adsorption of CO₂

Xuecong Ma^{*,†}, Linlin Geng^{✉*}, Yu Li^{*,†}, Jianwen Wei^{✉*,†,‡},
Lei Liao^{*,†} and Dunqiu Wang^{*,†}

**Guangxi Scientific Experiment*

*Center of Mining, Metallurgy and Environment
Guilin University of Technology, Guilin, P. R. China*

*†Guangxi Collaborative Innovation Center
for Water Pollution Control and Water Safety in Karst Area
Guilin, Guangxi 541004, P. R. China*

‡jianwen988@126.com

Received 17 June 2023

Accepted 11 March 2024

Published 18 April 2024

Micro/mesoporous materials are low-cost functional materials with the potential for CO₂ adsorption. Modifying micro/mesoporous materials is significant for enhancing CO₂ adsorption and their high-value utilization. Herein, the micro/mesoporous material of composite molecular sieve ZSM-5/MCM-48 (ZM) was synthesized by a two-step crystallization method using cetyltrimethylammonium bromide as a template, tetraethyl orthosilicate as a silicon source and ZSM-5 seed as part of silicon aluminum source. Tetraethylenepentamine (TEPA) and polyethyleneimine (PEI) were used as impregnation modifiers to modify ZM with amine groups. The results showed that with the increase of amine loadings, both ZM-T60 (Impregnated with TEPA) and ZM-P60 (Impregnated with PEI) functionalized adsorbents exhibited the best adsorption capacities of 4.97 mmol·g⁻¹ and 3.28 mmol·g⁻¹ at 60, respectively, when the loading of ZM sample was 60%. The adsorption kinetic analysis showed that the adsorption of CO₂ by ZM-T60 and ZM-P60 was a chemisorption-dominated process accompanied by physical adsorption. After 10 adsorption/desorption cycles, the CO₂ adsorption capacity of ZM-T60 and ZM-P60 decreased by 8.7% and 2.6%, respectively. This work demonstrates that impregnation modification of the composite molecular sieve to achieve efficient CO₂ adsorption has practical application significance.

Keywords: CO₂ adsorption; ZSM-5/MCM-48; amine impregnation modification; adsorption kinetics.

1. Introduction

Due to the increasing combustion of fossil fuels and the ensuing large-scale CO₂ emissions, the high CO₂ content in the global atmosphere is believed as the main driving force of global climate change, which may cause climate disasters, seriously affecting human life and the earth's ecology.¹ Once upon

a time, 195 member states reached the Paris Agreement at the Paris Climate Change Conference, which not only established a global action plan but also provided a bridge between today's policies and the climate goals for the end of the century, as the task of curbing global warming has become urgent.² Because of the large amount of

[‡]Corresponding author.

CO₂ emissions caused by the increase of fossil fuel combustion, it has promoted extensive research on CO₂ emission reduction planning and management. Carbon (more precisely, CO₂) capture and storage (CCS) and carbon capture and utilization (CCU) have become potential solutions to control CO₂ emissions.³ CCS can achieve significant CO₂ reductions in power systems because of its adaptability to existing energy systems and its stable operation.²

The primary techniques for capturing CO₂ post-combustion are absorption, membrane separation, low-temperature distillation, and adsorption. Absorption methods are classified into physical and chemical methods.^{4,5} Physical absorption relies on intermolecular forces, such as van der Waals forces, to capture CO₂. Chemical absorption, on the other hand, uses amine solution absorbents to react with CO₂. However, absorption methods have drawbacks such as high energy consumption for regeneration, equipment corrosion, and high cost. Membrane separation is a method of different interaction forces between different gases and membrane materials to achieve gas separation.⁶ However, the selection of membrane materials for separation and the high cost of this method hinders its large-scale application. In addition, the presence of impurity gases can affect the membrane CO₂ capture separation.⁷ Cryogenic distillation is a method of separating CO₂ from flue gases by liquefying the gas mixture by compression and multistage condensation and then physically distilling it according to the different boiling points of the various components.⁸ However, the high cost of this process, the large size of the equipment, the high energy consumption, the low separation efficiency and the susceptibility to interference from flue gas impurities limit its use. Adsorption^{9,10} is a capture method that uses the interaction force on the surface of a solid adsorbent to adsorb CO₂ on the solid surface, which can be divided into physical adsorption and chemical adsorption. Physical adsorption has the characteristics of fast adsorption speed, weak force and easy desorption, etc. Chemical adsorption is to use the functional groups on the surface of the adsorbent and CO₂ to have a chemical reaction to form a new substance to achieve the goal of capturing and separating CO₂. Chemical adsorption has the advantages of faster adsorption and diffusion rate, higher stability and higher selectivity.

Generally speaking, we use solid adsorbents to capture and separate CO₂ in flue gas.¹¹ Materials used for adsorption are generally divided into four

categories: (I) carbon-based materials,¹² (II) silica/alumina/zeolite,¹³ (III) porous crystal solids¹⁴ and (IV) metal oxides.¹⁵ Solid adsorbents have relatively little impact on the environment and health, with high adsorption capacity, low capital investment and easy handling. Therefore, solid adsorbents are one of the most promising candidates for CCS after combustion.¹¹ Common solid porous materials include Metal-Organic Framework (MOF),¹⁶ zeolites,¹⁷ activated carbon,¹⁸ molecular sieves,¹⁹ etc. Mesoporous materials²⁰ are mostly Santa Barbara Amorphous (SBA) series,²¹ Mobil Composition of Matter, Mobil Crystalline Materials (MCM) series²² and Mesoporous silica (KIT) series.²³ Porous materials have large pore volumes, accessible active sites and tunable functionality, and their structural diversity, mesoporous materials should hold great promise for the future in terms of integrated capture and utilization of flue gas or atmospheric CO₂.²⁴ Microporous materials are mostly zero synchronous modulation (ZSM) series,²⁵ 13X series,²⁶ β series, Y series,²⁷ Zeolitic Imidazolate Frameworks (ZIF) series²⁸ and ultra-microporous covalent-organic framework (COF) series.²⁹ Microporous organic polymers are also potential candidates for CO₂ capture materials, which have good physical-chemical stability and high specific surface area.³⁰

Since mesoporous materials and microporous materials have their own shortcomings in adsorbing CO₂, it is necessary to use composite materials to adsorb CO₂ to make up for their shortcomings. Some studies have also confirmed this point such as ZSM-5/SBA-16,^{31,32} ZSM-5/KIT-6,³³ β /KIT-6,^{34,35} Several composites are suitable for CCUS, such as silica/Mg-Al,³⁶ KIT-6/reduced graphene oxide,³⁷ Metakaolin/Brushite Hybrid Polymeric Composite Materials.³⁸ The composite adsorbents have good surface properties in terms of specific surface area, pore characteristics, adsorption capacity and high-temperature stability. Excellent performance can be achieved through activation or functionalized surface modification. Studies show that the functional composite materials provide surface properties in terms of specific surface area, micropore rate and high adsorption capacity of CO₂.³⁹ In addition, it was also found that amine group modification of these solid materials can obtain better adsorption performance.⁴⁰ CO₂ adsorption performance varies when modified with different amines.⁴¹

Although ZSM-5 and MCM-48 have been extensively studied as CO₂ adsorbents, there are few reports on ZSM-5/MCM-48 (ZM) and its modification by impregnation. Li *et al.*⁴² also reported microcross-pore composite HZSM-5/MCM-41 using *in situ* synthesis with HZSM-5 zeolite as the core and MCM-41 as the shell. Popova *et al.*⁴³ prepared composites of ZSM-5/KIT-6 and ZSM-5/SBA-15 with a mesoporous skeleton and zeolite stability using a post-synthesis method. Microporous regions were found in the mesoporous structure of both KIT-6 and SBA-15. Lin *et al.*⁴⁴ selected modified ZSM-5/KIT-6 composites impregnated with tetraethylenepentamine (TEPA) and polyethyleneimine (PEI) to achieve the highest CO₂ adsorption at 60°C (5.32 mmol · g⁻¹) and 75°C (4.59 mmol · g⁻¹), respectively. In terms of composite selection and synthesis methods used by others, there are still some shortcomings. However, some foundations have been laid for us to further synthesize new composites. In this research, ZSM-5/MCM-48 molecular sieves were prepared by a two-step crystallization method,⁴⁵ and the composites were modified with TEPA/PEI in an amine base. Compared to other types of mesoporous molecular sieves, the MCM-48 mesoporous molecular sieve exhibits superior material transport performance due to its two mirror-symmetric and mutually nonintersecting three-dimensional pore structures. This feature effectively prevents guest molecules from blocking the pores. However, the pore wall of MCM-48 is thin and its stability is poor. To address this issue, ZSM-5 species were introduced into the pore wall of the mesoporous material. This resulted in partial crystallization of the amorphous pore wall of the mesoporous molecular sieves, which increased their hydrothermal stability. Combined with the characterization, the CO₂ adsorption performance of the adsorbents was studied, and the optimal parameters of adsorption conditions were obtained. Then, the superior performance of the composite ZSM-5/MCM-48 and the kinetic law was investigated.

2. Experimental Methods

2.1. Preparation of ZSM-5/MCM-48

Using cetyltrimethylammonium bromide (CTAB, AR, Aladdin) as a template, tetraethyl orthosilicate (TEOS, AR, Aladdin) as a silicon source, and

ZSM-5 seed crystal as a part of the silicon aluminum source, a composite molecular sieve ZM with a regular pore structure and a large specific surface area and pore volume was synthesized by a two-step crystallization method. The specific preparation process is divided into the following steps.

First, 1.0 g of sodium meta-aluminate (NaAlO₂, AR, Aladdin) was dissolved in 20 mL of 1 M sodium hydroxide solution, and stirred for 1 h at 25°C to obtain the solution denoted as X. Then, 0.6 g of sodium hydroxide (NaOH, AR, Aladdin) and 5.3 g of tetrapropylammonium hydroxide (TPAOH, AR, Aladdin) were dissolved in 16 g of deionized water, stirred well to obtain the solution Y. Finally, solutions X and Y were mixed, stirred (25°C, 3 h), crystallized (170°C, 32 h), cooled, filtered, washed, dried and calcined (550°C, 6 h), which was synthesized by hydrothermal method to obtain the sample as ZSM-5.⁴⁶

Next, 10 mL of ethyl orthosilicate was put into 50 mL of deionized water, and stirred for 30 min at 25°C. Subsequently, 0.9 g of sodium hydroxide and 10.61 g of hexadecyltrimethylammonium bromide were added in sequence after complete dissolution, and stirred for 60 min, crystallized at 120°C for 36 h, vacuum filtered, washed, dried at 80°C for 12 h, and calcined at 550°C for 6 h. So MCM-48 was obtained.

Finally, 5.5 mL of tetraethylammonium hydroxide (C₈H₂₁NO, 25 wt.%, AR, Aladdin) was dispersed in deionized water, 10 mL of ethyl orthosilicate was dripped slowly and stirred for 30 min at 25°C. Subsequently, 0.1145 g of aluminum isopropoxide (AIP, AR, Xilong Chemical Co., Ltd.) was added to the above solution and stirred for 2 h at 25°C, and then reacted at 100°C in the reactor. After 4 h, the cooled solution was recorded as A. Then, 0.9346 g of sodium hydroxide was added to deionized water, and 1.9818 g of cetyltrimethylammonium bromide was added after its complete dissolution, and then solution A was dripped slowly dropwise, stirred (45°C, 2 h), crystallized (150°C, 8 h), cooled to 25°C and filtered, dried (100°C, 24 h), and calcined (550°C, 6 h). Eventually, the solid product ZSM-5/MCM-48 (ZM) was obtained by a two-step crystallization method.^{47,48}

2.2. Preparation of amine-impregnated samples

Tetraethylenepentamine (CP, Sinopharm Chemical Reagent Co., Ltd.) or polyethyleneimine

(AR, Aladdin) was immersed into ZM carrier. The specific operation was as follows: First, a certain amount of TEPA/PEI was added into 25 mL ethanol and stirred for 30 min to fully dissolve it. Subsequently, 0.5 g dried ZM was put into the above solution, stirred for 6.5 h, then evaporated and dried in an oven at 80°C for 10 h to obtain a solid. Then the oven temperature was increased to 100°C for 2 h until the solid was dried. The obtained product is named ZM-TX or ZM-PX ($X = 40, 50, 60$, or 70 , where X represents the mass fraction of impregnated modified TEPA/PEI).

2.3. Characterization

The XRD characterization was carried out by a desktop X-ray diffractometer (X'Pert3 Power). CuK α was used as the radiation source, with a scan step of 0.03°, a tube voltage of 40 kV, a tube current of 40 mA, a small-angle scan range of $2\theta = 0.6$ – 10° and a wide-angle scan range of $2\theta = 10$ – 80° with a scanning speed of $10^\circ \text{ min}^{-1}$, respectively.

The morphology of each sample was obtained by scanning electron microscopy with a JSM-7900F scanning electron microscopy (HI-TACHI, Japan). Before the test, the sample was dried (80°C, 12 h), uniformly dispersed in anhydrous ethanol by ultrasonic oscillation, and then loaded on the surface of copper mesh and dried at room temperature.

The modified functional groups of ZM samples were analyzed by Nexus 470 Fourier infrared spectrometer. Before the test, the sample was prepared by thorough grinding with KBr at a ratio of 1:100. The scanning wavenumber range is 400–4000 cm^{-1} .

The thermal stability was measured with an SDT Q600 Thermogravimetric analyzer. In the nitrogen atmosphere, the temperature was increased to 800°C at the rate of $5^\circ\text{C} \cdot \text{min}^{-1}$ and the weight change of the sample was analyzed.

The specific surface (calculated by BET multipoint method, $P/P_0 = 0.05$ – 1.0), pore volume ($P/P_0 = 0.99$), and pore diameter (calculated by BJH desorption method) of the sample were tested by low-temperature N_2 absorption desorption method. The measurement was carried out by a specific surface area analyzer (JW-BK200C) at liquid nitrogen temperature (77 K). The samples before the test were degassed in a vacuum (100°C, 2 h).

The nitrogen content in the sample is obtained by an EA 2400 II element analyzer.

2.4. CO_2 adsorption

The CO_2 adsorption performance and cycle stability of the samples were measured by the SDT-Q600 synchronous thermal analyzer (TA, US). Before the experiment, the samples were dried in an oven at 100°C for 8 h in advance. Around 6 mg of adsorbent was heated up to 110°C in a nitrogen atmosphere at a heating rate of $10^\circ\text{C min}^{-1}$ and kept for 50 min to remove the water vapor and other impurity gases to get a constant weight. After that, the sample was cooled to 60°C before exposure to the CO_2/N_2 mixed gases (15 vol.% CO_2) until the weight of the sample displayed no noticeable changes. The adsorption capacities of samples were calculated using the following equation:

$$q_e = \frac{(m_e - m_d)/44.01}{m_d/1000}, \quad (1)$$

where q_e is CO_2 saturation adsorption capacity, $\text{mmol} \cdot \text{g}^{-1}$; m_e is weight of the sample after adsorption, mg; m_d is weight of the sample after removing water and impurity gas, mg.

In the cyclic stability test (60°C, 120 min), the sample was heated under N_2 purging (110°C, 40 min) to remove the adsorbed CO_2 . The cycle was carried out 10 times to explore the cyclic performance.

3. Results and Discussion

3.1. Characterization of samples

As can be seen from Fig. 1, the crystal structures of MCM-48, ZSM-5, ZM, ZM-T60 and ZM-P60 samples were tested by powder XRD. Figure 1(a) shows the XRD small-angle patterns of the samples with a strong diffraction peak at $2\theta = 2.6^\circ$ and 3.0° , respectively, corresponding to the (211) and (220) diffraction peaks of MCM-48. The characteristic diffraction peaks of MCM-48 mainly appear in 3–6°, corresponding to (321), (400), (420) and (332) planes, respectively. The characteristic diffraction peaks of ZSM-5 mainly appear in 8–9°, corresponding to (101) and (200) planes, respectively, corresponding to Fig. 1(b). After ZSM-5 was added, the diffraction peak intensity decreased significantly and the unit cell parameters decreased, which indicated that adding ZSM-5 would affect the ordering of the mesoporous structure of MCM-48, but the cubic pore structure was not completely destroyed. Due to the large relative intensity of the peaks at MCM-48, the peaks at (101) and (200) are less

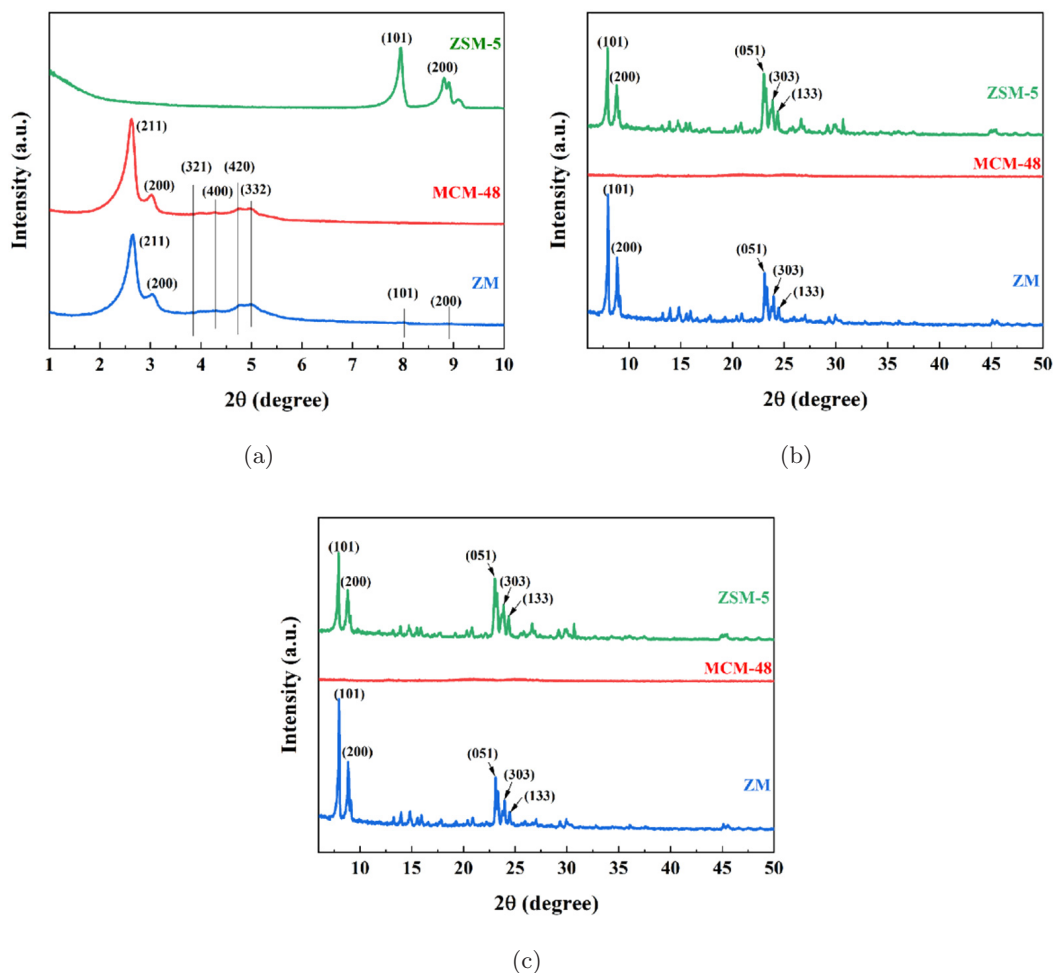


Fig. 1. (a) Small-angle and (b) Wide-angle patterns of ZSM-5, MCM-48, ZM, (c) Wide-angle patterns of ZM-T60 and ZM-P60.

pronounced in the ZM. Figure 1(b) shows the XRD wide-angle patterns of the samples. MCM-48 is made of porous silicon dioxide. Typically, it only displays clear diffraction peaks in the low-angle region, with no peaks beyond ten degrees (refer to JCPDS No. 49-1712 for the diffraction peaks of standard silica). ZM has diffraction spikes at $2\theta = 7.9^\circ, 8.8^\circ, 23^\circ, 23.6^\circ$ and 24.3° , which correspond to the (101), (200), (051), (303) and (133) crystal planes of the ZSM-5 samples, respectively.⁴⁹ The composite material ZM has been successfully prepared. Figure 1(c) displays the XRD large-angle view of samples ZM-T60 and ZM-P60 after modifying the composite ZM through impregnation with TEPA and PEI. After modification, the TEPA/PEI modified impregnation only covers the surface of the sample. The diffraction peaks of the modified material and ZM are almost identical in the XRD test because X-rays are strong and penetrate through the material.

Figure 2(a) shows that ZSM-5 has uniform spherical particles formed by stacking cubic sheets. With high crystallinity, it is consistent with the XRD analysis shown in Fig. 1. The cubic phase MCM-48 molecular sieve in Fig. 2(b) is composed of submicron-sized aggregated spherical particles.⁵⁰ There are two types of particles in ZM material⁵¹ [Fig. 2(c)], which are also found in Figs. 2(a) and 2(b). SEM images of the amine-based modifier TEPA and TEPA loaded onto ZM are shown in Figs. 2(d) and 2(e), respectively. Compared with Fig. 2(c), it is evident that ZM is covered with the amine-based modifier, resulting in a rougher surface, indicating successful loading onto the carrier ZM. Additionally, due to its large molecular weight, PEI is more likely to cause agglomeration and block the pores on the surface. Figure 2(f) is the transmission electron microscope pattern of ZM. The pores of ZM with both MCM-48 and ZSM-5 were better ordered with pore sizes of about 2.7 nm and 0.55 nm,

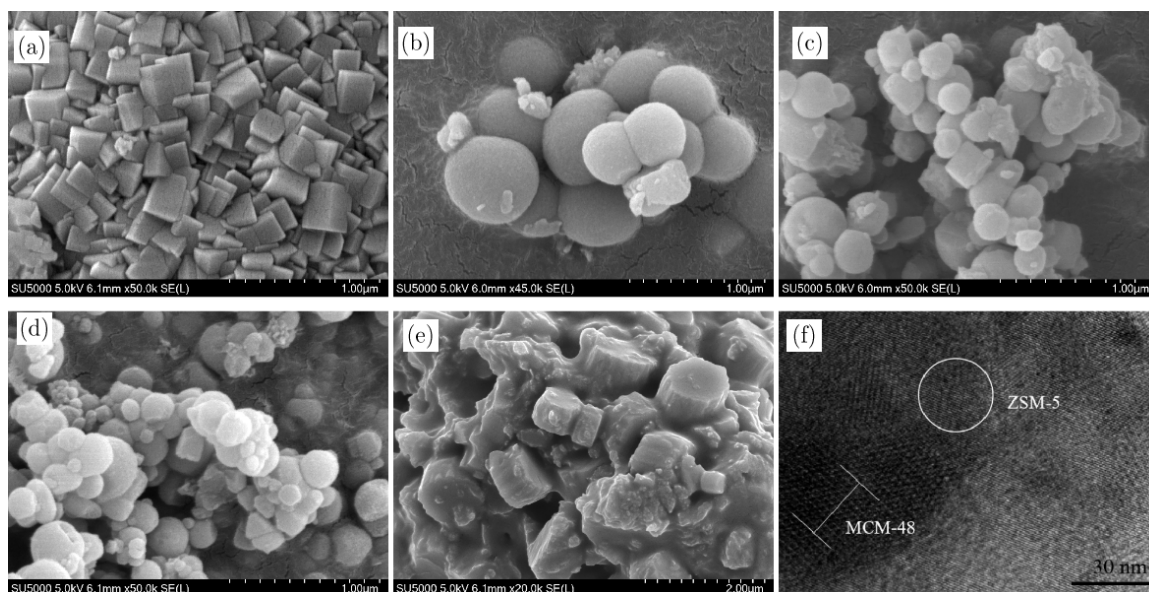


Fig. 2. Scanning Electron Microscopy (SEM) diagrams of (a) ZSM-5, (b) MCM-48, (c) ZM, (d) ZM-T60, (e) ZM-P60 and (f) Transmission Electron Microscope (TEM) diagrams of ZM.

respectively, which shows that ZSM-5 and MCM-48 have been successfully compounded tighter.

The FT-IR spectra of ZM, ZM-T60 and ZM-P60 samples are shown in Fig. 3. All samples have peaks at 3466 cm^{-1} and 1638 cm^{-1} , of which the absorption peak at 3466 cm^{-1} is caused by the adsorbed water on the adsorbent surface and the O-H antisymmetric stretching vibration generated during immersion. The peak at 1638 cm^{-1} is due to the bending vibration of the O-H of the surface hydroxyl groups brought about by the adsorption of water and the modification.⁵² The peaks at 1099 cm^{-1} and 794 cm^{-1} were identified over all the samples because of the antisymmetric and symmetric stretching vibration of Si-O-Si or Si-O-Al groups in MCM-48. Compared with the original sample, the modified samples had four more characteristic peaks at 2952 cm^{-1} , 2849 cm^{-1} , 1567 cm^{-1} and 1478 cm^{-1} . The peaks at 2952 cm^{-1} and 2849 cm^{-1} were the symmetrical and antisymmetric peaks of the C-H bond of the methyl group on the modifier TEPA and PEI, respectively. The peaks at 1567 cm^{-1} and 1478 cm^{-1} were the N-H bending vibration peak of primary amine and the C-H bending vibration peak, respectively. The infrared spectrum analysis shows that the modifier TEPA and PEI have been successfully impregnated on ZM. Simultaneously, the silicon hydroxyl group on ZM reacted with the methoxy group in TEPA/PEI, forming a

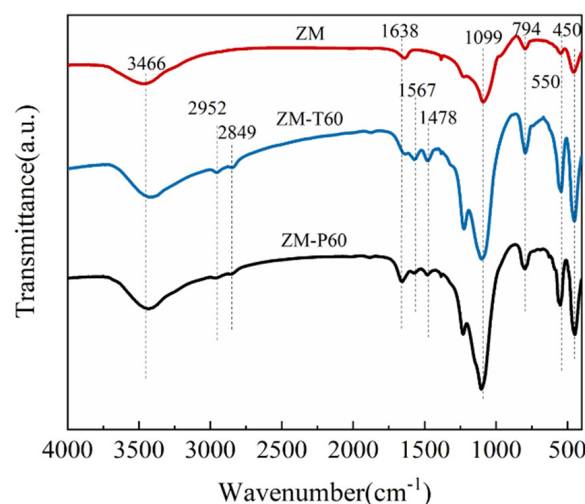


Fig. 3. The FT-IR spectra of ZM, ZM-T60 and ZM-P60.

siloxyl group. This reaction consumed a portion of the Si-OH group-impregnated samples, resulting in a weaker peak at 1638 cm^{-1} .

It can be seen from Fig. 4 that the first weight loss stage occurs when the temperature rises to 100°C , because of the removal of the physically absorbed water and impurity gases in samples. ZM-TX ($X = 40, 50, 60$ or 70 , where X represented the mass fraction of impregnated modified TEPA/PEI) sample has a maximum weight loss rate of around 200°C , and the ZM-PX sample has a maximum weight loss rate of around 300°C . This is

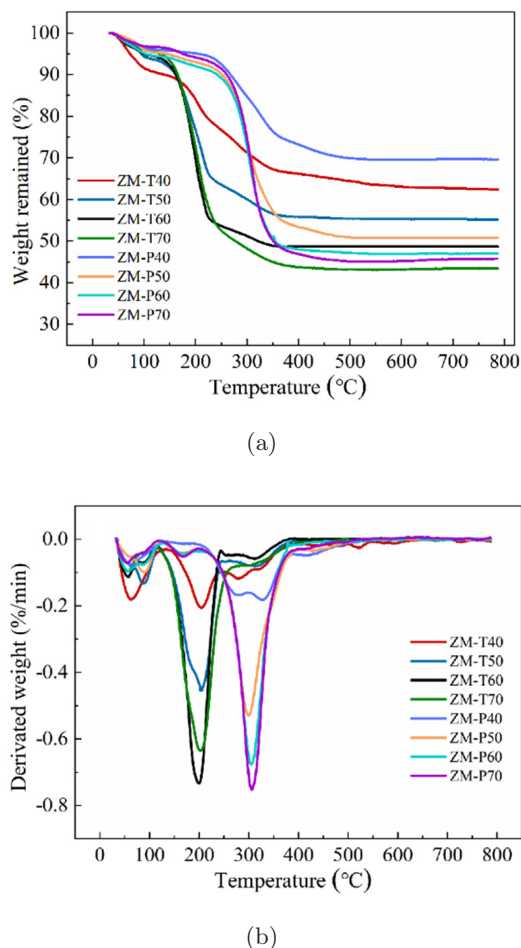


Fig. 4. (a) TGA curves and (b) DTG curves of TEPA and PEI-impregnated ZM.

because the ZM-PX sample has a higher decomposition temperature and thermal stability than the ZM-TX sample. With the amine loading increasing, the weight loss of the samples also increased gradually, ZM-T40, ZM-T50, ZM-T60 and ZM-T70 show weight loss of about 37.6%, 49.8%, 55.3% and 56.6%, respectively. When the modifier loading was low, the actual loading was closer to the theoretical loading. As the amount of modifier impregnation increases, the theoretical value differs from the actual value which may be due to the clogging of the pores of the sample and the saturation of the impregnation. Because both ZM-TX and ZM-PX samples exhibit thermal stability at 125 °C and 200 °C, respectively, 110 °C is used as the desorption temperature of the adsorption/desorption cycle.

Figure 5(a) shows that when the amine impregnation rate was lower, the adsorption/desorption isotherm curves of ZM-TX and ZM-PX samples were typical IV-type isotherms. This hysteresis loop

was an H1-type hysteresis loop and belonged to a mesoporous material. With the increase of the loading of amine, the pores will be partially filled, and the hysteresis loop will become smaller and disappear. When the loading of TEPA and PEI increased from 40% to 70%, the specific surface area of ZM-TX samples decreased from $158.165 \text{ m}^2 \cdot \text{g}^{-1}$ to $4.506 \text{ m}^2 \cdot \text{g}^{-1}$, the specific surface area of ZM-PX samples decreased from $68.642 \text{ m}^2 \cdot \text{g}^{-1}$ to $4.122 \text{ m}^2 \cdot \text{g}^{-1}$, and the mesopore volume decreased from $0.218 \text{ m}^2 \cdot \text{g}^{-1}$ and $0.191 \text{ m}^2 \cdot \text{g}^{-1}$ to $0.037 \text{ m}^2 \cdot \text{g}^{-1}$ and $0.031 \text{ m}^2 \cdot \text{g}^{-1}$, respectively. Figure 5(b) shows the pore size distribution of modified ZM impregnated with amine. Combined with the analysis of XRD plots, it is evident that ZM possesses a regular and single mesoporous skeleton structure. The pore wall of the mesoporous molecular sieve has been

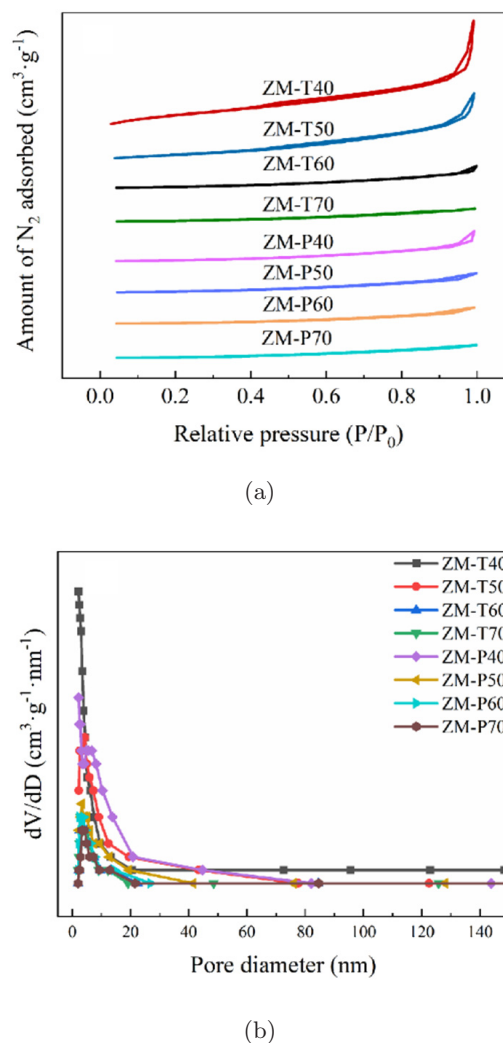


Fig. 5. (a) N₂ adsorption/desorption isotherms of amine-impregnated ZM and (b) Pore size distribution of amine-impregnated ZM.

Table 1. Physical properties, nitrogen content, CO₂ adsorption capacity and amine efficiency of adsorbents at 60°C.

Adsorbent	Pore volume BJH (cm ³ · g ⁻¹)	Surface area BET (m ² · g ⁻¹)	N content (mmol · g ⁻¹)	Adsorption capacity (mmol · g ⁻¹)	Amine efficiency (mmol CO ₂ /mmol N)
ZSM-5	0.104	110.200	0.34	0.89	2.62
MCM-48	1.451	1240.700	0.15	0.73	4.87
ZM	0.888	954.00	0.29	0.99	3.41
ZM-T40	0.218	158.165	6.34	2.54	0.40
ZM-T50	0.116	25.640	8.66	3.51	0.41
ZM-T60	0.053	7.619	10.85	4.97	0.46
ZM-T70	0.037	4.506	12.67	4.63	0.37
ZM-P40	0.191	68.642	7.87	1.77	0.22
ZM-P50	0.097	22.604	9.46	2.65	0.28
ZM-P60	0.036	3.735	11.50	3.28	0.29
ZM-P70	0.031	4.122	13.36	2.26	0.17

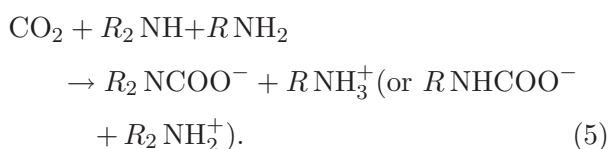
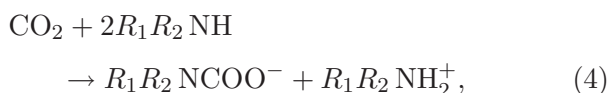
modified to introduce a microporous structure. The pore size of ZM decreases with an increase in the amine-based modifier. This decrease is attributed to the introduction of amine groups during impregnation modification, which also results in pore blockage if the impregnation modifier is excessive.

The content of the amine group in the functional adsorbent can be expressed by the content of the N element. The amine efficiency of the adsorbent can be calculated from the analysis results of the N element, and the equation is as follows:

$$\text{Amine efficiencies} = \frac{n\text{CO}_2}{n\text{N}}. \quad (2)$$

$n\text{CO}_2$ is saturated adsorption capacity of CO₂, mmol · g⁻¹; $n\text{N}$ is molar content of element N in sorbent, mmol · g⁻¹.

Amine organic compounds have three types of amine groups: primary, secondary and tertiary amines, respectively, which can react with CO₂, and only primary and secondary amines will react with CO₂ under dry conditions, with the following reaction equations:



The amine groups in TEPA and PEI are primary and secondary amines. Due to the introduction of -NH₂ after the amine-based impregnation of the

modified adsorbent ZM, the affinity of the sample for CO₂ is increased, and the primary amine generates carbamate with CO₂ under dry conditions, as shown in Eq. (3). According to the reaction equations, the maximum theoretical load of 1 mol amine on CO₂ is 0.5 mol, so the maximum theoretical amine efficiency (CO₂/N, molar ratio) is 0.5.

Table 1 summarizes the N content of TEPA and PEI functional adsorbents, as well as the CO₂ adsorption capacity and amine efficiency at 60°C. It can be seen from Table 1 that as the TEPA/PEI impregnation increased, the N content of ZM-TX also gradually increased. The N content of ZM-TX increased from 6.34 mmol · g⁻¹ to 12.67 mmol · g⁻¹, and that of ZM-PX increased from 7.87 mmol · g⁻¹ to 13.36 mmol · g⁻¹.

3.2. CO₂ adsorption performance

Figure 6 shows that the ZM-TX samples were better than the ZM-PX samples. The CO₂ saturation adsorption capacity was 4.97 mmol · g⁻¹ for ZM-T60 and 3.28 mmol · g⁻¹ for ZM-P60. When the loading of TEPA or PEI increased from 40% to 60%, the corresponding CO₂ adsorption capacity increased from 2.94 mmol · g⁻¹ and 1.77 mmol · g⁻¹ to 4.97 mmol · g⁻¹ and 3.28 mmol · g⁻¹, respectively. When the loading on ZM increased from 60% to 70%, the CO₂ saturation adsorption capacity was instead reduced to 4.63 mmol · g⁻¹ and 2.26 mmol · g⁻¹. This was because as the concentration of the modifier continued to increase, the excess TEPA and PEI partially blocked the pores and made it difficult for CO₂ to have access to the amino active sites, so the adsorption capacity decreased.

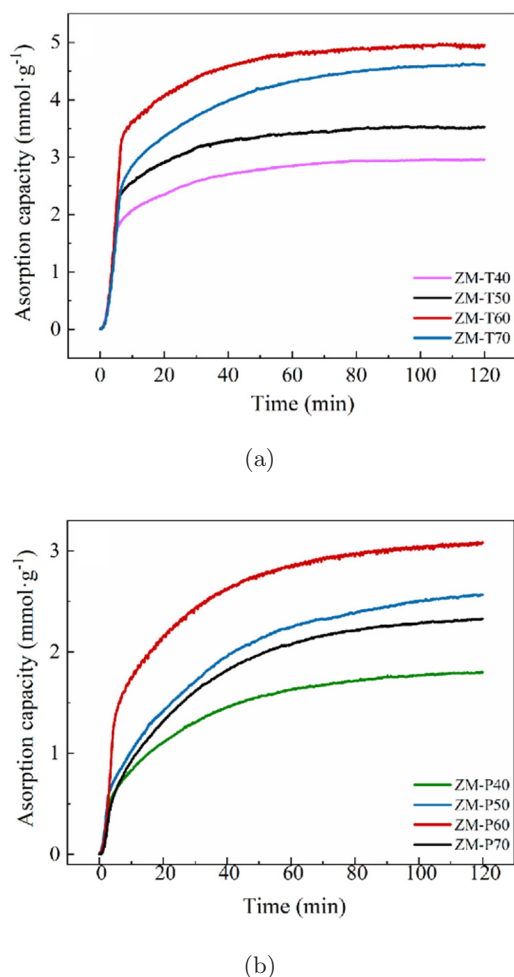


Fig. 6. (a) CO₂ adsorption curves of ZM-TX and (b) CO₂ adsorption curves of ZM-PX.

Moreover, it was found that the CO₂ saturation adsorption capacity of TEPA-impregnated adsorbent was better than that of PEI-impregnated. This was because that TEPA is a linear polymeric amine with a relatively small molecular weight, so its molecules dispersed well into the pores of ZM, and the CO₂ saturation adsorption capacity of ZM-TX was better than that of ZM-PX at the same loading.

Similarly, the adsorption temperature is an important factor that affects the adsorption capacity of CO₂. The adsorption experiments of ZM-T60 and ZM-P60 on CO₂ were carried out at 30, 45, 60, 75 and 90°C. In the range of 30–90°C, the saturation adsorption capacity of CO₂ tends to increase and then decrease with the increase in temperature, and the maximum saturation adsorption amount happens at 60°C. The adsorption capacity increases in the temperature range of 30–60°C.

On the one hand, at lower temperatures, the viscosity of the amine compounds on the surface of the carrier was high and agglomeration tended to occur. As the temperature increases, the molecular activity of the amine modifier increases and is uniformly dispersed on the carrier surface and pore channels, resulting in more amine-based active sites. On the other hand, when the temperature is lower, the diffusion resistance of CO₂ is higher and the spatial potential resistance effect is significant. With the increase in temperature, the kinetic energy of CO₂ molecules increases, which reduces the diffusion resistance and increases the probability of reaction with amino active sites. At 60–90°C, the adsorption capacity decreases with increasing temperature. In terms of adsorption thermodynamics, the reaction of amine-impregnated adsorbent to CO₂ was exothermic, higher temperature will inhibit the reaction of amine group with CO₂. On

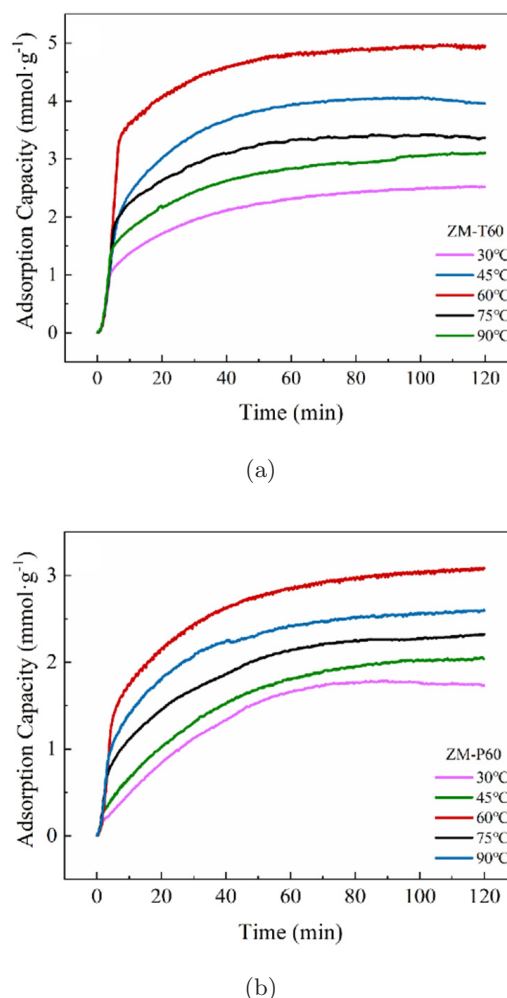


Fig. 7. CO₂ adsorption curves of (a) ZM-T60 and (b) ZM-P60 at different temperatures.

Table 2. CO₂ adsorption capacities of various adsorbents from literature and our work.

Support	Modifier	Modification method	Temperature (°C)	CO ₂ concentration	CO ₂ adsorption capacity (mmol · g ⁻¹)
HZSM-5	AEEA	Impregnation	20	10 vol.% CO ₂	4.44 ⁵³
HZSM-5	MEA	Impregnation	20	10 vol.% CO ₂	4.27 ⁵³
Fumed silica	PEI	Impregnation	70	99.9 vol.% CO ₂	3.24 ⁵⁴
MF/PAM-g	PEI	Impregnation	0	10 vol.% CO ₂	2.8 ⁵⁵
MCM-41	PEI	Impregnation	25	99.9 vol.% CO ₂	3.53 ⁵⁶
ZSM-5/MCM-48	TEPA	Impregnation	60	15 vol.% CO ₂	4.97 (This work)
ZSM-5/MCM-48	PEI	Impregnation	60	15 vol.% CO ₂	3.28 (This work)

the other hand, as the temperature increases, the CO₂ molecules become more likely to overcome the van der Waals and electrostatic forces between them and the surface of the adsorbent, resulting in a decrease in adsorption.

The equilibrium adsorption amounts of ZM-T60 were 2.51, 3.95, 4.96, 3.36 and 3.10 mmol · g⁻¹ at 30, 45, 60, 75 and 90°C, respectively, while the adsorption amounts of ZM-P60 were 1.74, 2.04, 3.08, 2.59 and 2.32 mmol · g⁻¹, respectively.

Table 2 shows the CO₂ adsorption amounts of various amine-impregnated adsorbents. Cheng *et al.*⁵³ modified HZSM-5 with AEEA and MEA modifiers and adsorbed 10 vol.% CO₂ at 20°C. The adsorption amounts were 4.44 mmol · g⁻¹ and 4.27 mmol · g⁻¹ for Aminoethylethanolamine (AEEA) and monoethanolamine (MEA), respectively. Goeppert *et al.*⁵⁴ modified fumed silica impregnated with PEI adsorbed CO₂ (99.9 vol.% CO₂) at 70°C and obtained adsorption of 3.24 mmol · g⁻¹. Yin *et al.*⁵⁵ investigated the adsorption of CO₂ (10 vol.% CO₂) using a PEI-modified nitrogen-rich polymer network (MF/PAM-g) at 0°C, achieving a capacity of 2.8 mmol · g⁻¹. Rao *et al.*⁵⁶ modified MCM-41 with polyethyleneimine (PEI) and adsorbed carbon dioxide (99.9 vol.%) at 25°C, achieving an adsorption capacity of 3.53 mmol · g⁻¹. The effect of adsorption is influenced by the temperature of adsorption and the concentration of carbon dioxide. Under similar conditions, both ZM-T60 and ZM-P60 obtained in this work showed better adsorption performance compared to other adsorbents.

Pseudo-first-order kinetic model, pseudo-second-order kinetic model and Avrami model are often used to simulate the adsorption reaction mechanism of gas on the surface of solid materials. In this experiment, these three models were also

used to fit and analyze the CO₂ adsorption data of various adsorbents.

Pseudo-first-order kinetic model, pseudo-second-order kinetic model and Avrami model are shown as follows:

$$q_t = q_e(1 - e^{-k_1 t}), \quad (6)$$

$$\frac{t}{q_t} = \frac{1}{k_2 q_e^2} + \frac{t}{q_e}, \quad (7)$$

$$q_t = q_e[1 - e^{-(k_A t)^{n_A}}], \quad (8)$$

where q_t is CO₂ adsorption capacity of the adsorbent at time t , mmol · g⁻¹; q_e is saturated adsorption capacity of adsorbent, mmol · g⁻¹; k_1 is pseudo-first-order kinetic rate constant, g · mmol⁻¹ · min⁻¹; k_2 is pseudo-second-order kinetic rate constant, min⁻¹; k_A is Avrami model rate constant, min⁻¹; n_A is Avrami model series.

The adsorption data of ZM-T60 and ZM-P60 at different temperatures were fitted by the three above models. Figures 8–10 show the fitting results of ZM-T60 and ZM-P60 at 30, 45, 60, 75 and 90°C, respectively. The specific fitting parameters are presented in Table 3.

From Fig. 8, the fitting curve of the pseudo-first-order kinetics that the correlation coefficients R^2 fitted to the data of the ZM-T60 and ZM-P60 samples at 60°C were slightly low, indicating that the pseudo-first-order kinetics equation cannot describe well the adsorption reaction process of ZM-T60 and ZM-P60 for CO₂, revealing that the adsorption process may not be purely physical adsorption.

The saturated CO₂ adsorption amounts fitted by the pseudo-second-order kinetic model were all greater than the experimentally measured adsorption amounts. From Fig. 9, it can be seen the saturated CO₂ adsorption amounts fitted by

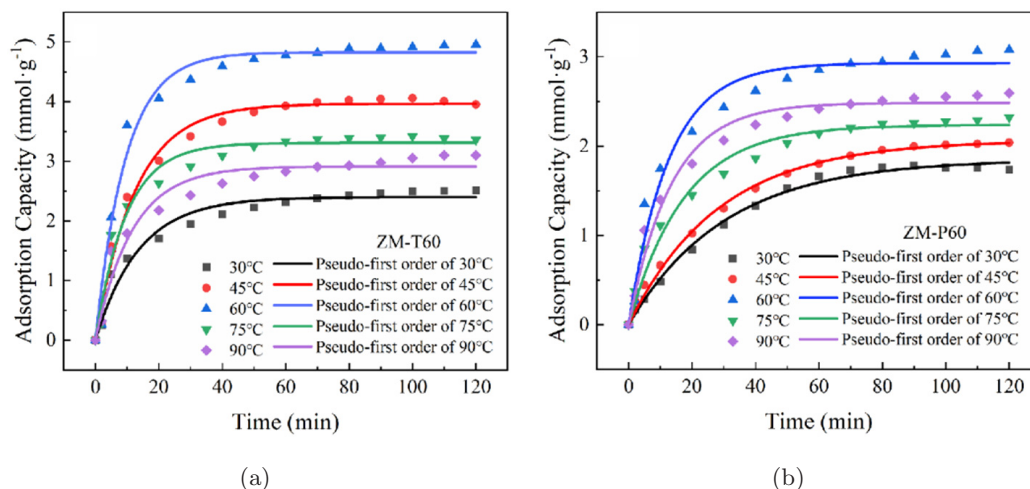


Fig. 8. Pseudo-first-order fitting curves of (a) ZM-T60 and (b) ZM-P60 at various temperatures.

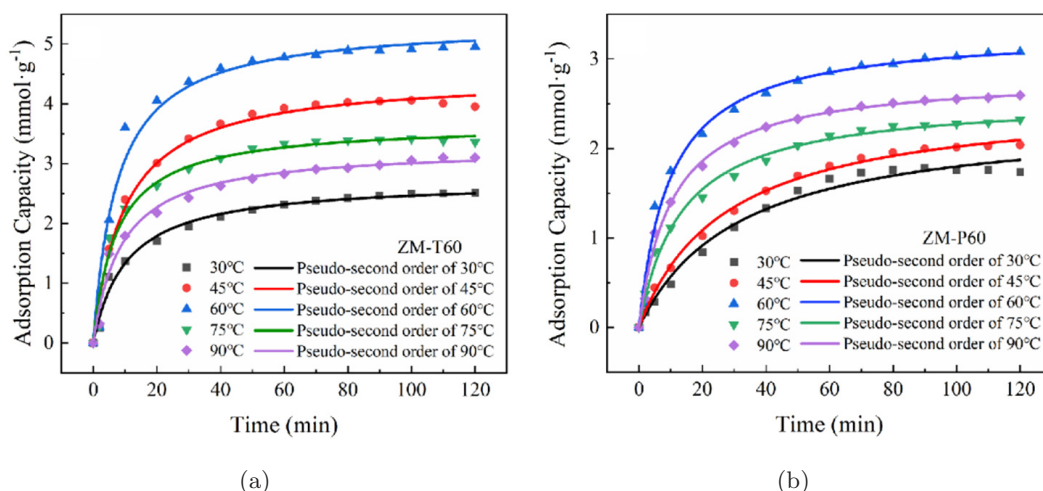


Fig. 9. Pseudo-second-order fitting curves of (a) ZM-T60 and (b) ZM-P60 at various temperatures.

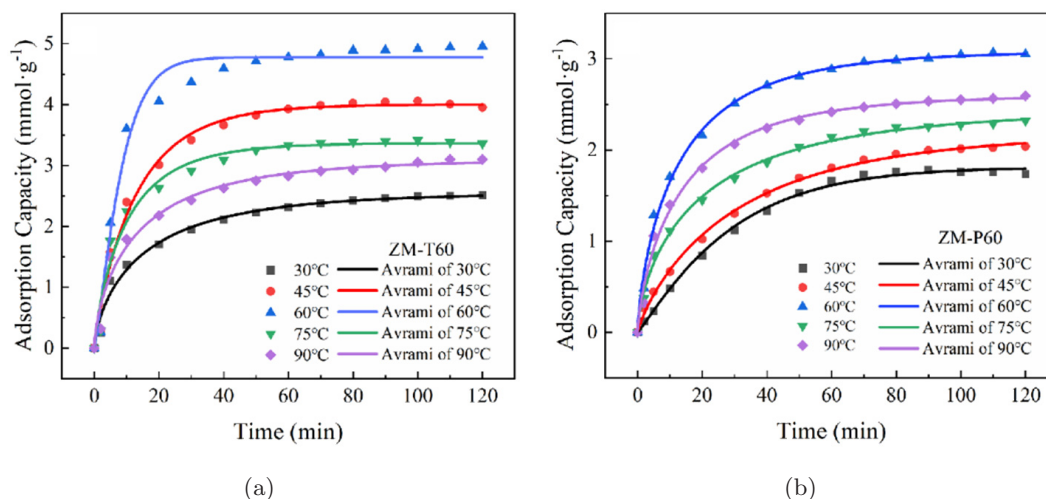


Fig. 10. Avrami fitting curves of (a) ZM-T60 and (b) ZM-P60 at various temperatures.

Table 3. Kinetics parameters of adsorption of CO₂ on ZM-T60 and ZM-P60 at various temperatures.

Model	Kinetics parameters	ZM-T60 (°C)					ZM-P60 (°C)				
		30	45	60	75	90	30	45	60	75	90
Pseudo-first order	q_e (mmol · g ⁻¹)	2.40	3.96	4.83	3.31	2.91	1.85	2.07	2.93	2.24	2.49
	k_1 (min ⁻¹)	0.0073	0.0079	0.105	0.104	0.086	0.033	0.035	0.079	0.058	0.074
	R^2	0.967	0.987	0.978	0.970	0.959	0.985	0.985	0.970	0.974	0.981
Pseudo-second order	q_e (mmol · g ⁻¹)	3.72	4.48	5.37	3.67	3.27	2.37	2.60	3.31	2.57	2.82
	k_2 (g · mmol ⁻¹ · min ⁻¹)	0.0035	0.023	0.025	0.037	0.034	0.013	0.014	0.031	0.029	0.035
	R^2	0.988	0.987	0.970	0.978	0.984	0.985	0.986	0.988	0.983	0.985
Avrami	q_e (mmol · g ⁻¹)	2.55	4.00	4.78	3.37	3.09	1.81	2.18	3.08	2.44	2.59
	k_A (min ⁻¹)	0.142	0.099	0.070	0.145	0.162	0.024	0.054	0.144	0.127	0.132
	n_A	0.695	0.901	0.722	0.822	0.681	0.899	0.841	0.729	0.700	0.741
	R^2	0.984	0.988	0.977	0.972	0.976	0.996	0.998	0.995	0.996	0.993

the pseudo-second-order kinetic model were all larger than the experimentally measured adsorption amounts, but the correlation coefficient R^2 was low. These results suggested that the pseudo-second-order kinetics model cannot describe well the CO₂ adsorption process of ZM-T60 and ZM-P60. Therefore, it is inferred that the adsorption process is not purely chemical adsorption.

From Fig. 10, the Avrami model can describe better the adsorption processes of ZM-T60 and ZM-P60 for CO₂. Therefore, the adsorption of CO₂ by impregnated modified ZM was a chemically dominated process with both chemical and physical adsorption, and the difference in n_A values was small, indicating a consistent adsorption mechanism at different temperatures.

3.3. Cycle performance

In practical applications, CO₂ adsorbents should have good cyclic adsorption/desorption performance and low cost, in addition to efficient adsorption performance and good stability performance. In this work, the cyclic adsorption/desorption performance of ZM-T60 and ZM-P60 were tested by TGA method. Figure 11 shows the results of 10 consecutive cyclic adsorption/desorption tests.

It can be seen from Fig. 11 that the saturated adsorption capacity of ZM-T60 and ZM-P60 decreased after 10 adsorption/desorption cycles. After 10 cycles of adsorption/desorption, the adsorption capacity of ZM-T60 was 4.525 mmol · g⁻¹, which was 8.7% less than the original one (4.956 mmol · g⁻¹). Similarly, the adsorption capacity of ZM-P60 was 3.006 mmol · g⁻¹, which was 2.6% less than the original one (3.087 mmol · g⁻¹).

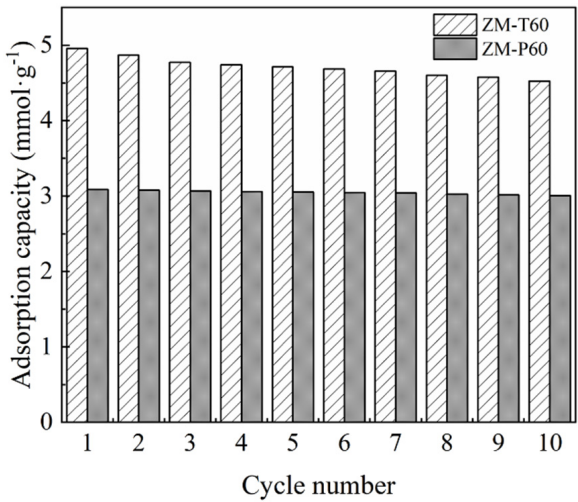


Fig. 11. The CO₂ saturated adsorption capacity of ZM-T60 and ZM-P60 during 10 times adsorption/desorption cycles.

The reason why ZM-P60 showed a lower saturated adsorption loss was that PEI is a polymer with high molecular weight and good thermal stability performance. In summary, after 10 adsorption/desorption cycles, the ZM-T60 adsorbent still had a high adsorption capacity. Therefore, the TEPA-impregnated adsorbent has a good application prospect.

4. Conclusion

CO₂ capture by adsorption is a promising method that involves developing CO₂ adsorbents with high capacity, selectivity, ease of regeneration, and low cost. Our adsorbent in this study has an optimum temperature of 60°C, making it suitable for capturing industrial flue gas at low temperatures

after combustion in practical applications. Composite molecular sieves ZM were prepared using a two-step hydrothermal crystallization method in this work. Physical impregnation was then used to load TEPA or PEI onto the ZM. The CO₂ adsorption/desorption performance and characteristics of ZM-TX or ZM-PX were studied. The saturated CO₂ adsorption capacity of the adsorbent increased initially with the increase of TEPA/PEI loading on the ZM carrier but then decreased. The maximum capacity for CO₂ adsorption for ZM-T60 and ZM-P60 is 4.97 mmol · g⁻¹ and 3.28 mmol · g⁻¹, respectively. The analysis of adsorption kinetics shows that both ZM-TX and ZM-PX adsorption processes can be described by the Avrami model. The fitted saturated adsorption amount of CO₂ was almost the same as the experimental value, indicating a good fit. This proves that the amine-impregnated composite ZM undergoes both physical and chemical adsorption processes. ZM-T60 and ZM-P60 were selected for adsorption/desorption cyclic tests. After 10 cycles, the saturated adsorption capacity of ZM-T60 decreased by 8.7% and that of ZM-P60 decreased by 2.6%. However, ZM-T60 still maintains a high-adsorption capacity and good stability. Therefore, the TEPA-impregnated adsorbent shows promise for future applications and warrants further investigation due to its superior performance and higher efficiency in CO₂ adsorption compared to the original composite.

Acknowledgments

The authors sincerely acknowledge the support of the National Natural Science Foundation of China (No. 51966002).

ORCID

Linlin Geng  <https://orcid.org/0000-0002-4464-6319>

Jianwen Wei  <https://orcid.org/0000-0002-8959-1462>

References

1. S. Liu, B. Sun, J. Xu, H. Li and X. Wang, *Geofluids* **2020**, 1 (2020).
2. H. Zeng, X. Qu, D. Xu and Y. Luo, *Front. Chem.* **10**, 939701 (2022).
3. W. N. R. Mohd Nawi, S. R. Wan Alwi, Z. A. Manan and J. J. Klemeš, *Clean Technol. Environ. Policy* **18**, 2227 (2016).
4. A. A. V. Julio, R. Castro-Amoedo, F. Maréchal, A. M. González and J. C. Escobar Palacio, *Energy* **280**, 128004 (2023).
5. L. Dubois and D. Thomas, *Chem. Eng. Technol.* **35**, 513 (2012).
6. J.-R. Li, Y. Ma, M. C. McCarthy, J. Sculley, J. Yu, H.-K. Jeong, P. B. Balbuena and H.-C. Zhou, *Coord. Chem. Rev.* **255**, 1791 (2011).
7. J. Xu, Z. Wang, Z. Qiao, H. Wu, S. Dong, S. Zhao and J. Wang, *J. Membr. Sci.* **581**, 195 (2019).
8. L. Zheng, K. Li, Q. Wang, G. Naidu, W. E. Price, X. Zhang and L. D. Nghiem, *Environ. Technol. Innov.* **22**, 101508 (2021).
9. L. D. S. Alves, B. R. D. A. Moreira, R. D. S. Viana, E. S. Dias, D. L. Rinker, A. Pardo-Gimenez and D. C. Zied, *Environ. Res.* **204**, 111945 (2022).
10. H. Cheng, D. Gong, T. Zhao, T. Wang and S. Jiang, *J. Phys. Conf. Ser.* **2076**, 012034 (2021).
11. O. Akeeb, *J. Environ. Manag.* **313**, 115026 (2022).
12. M. Bermeo, *Sci. Total Environ.* **810**, 151720 (2022).
13. W. W. Lestari, L. Yunita, T. E. Saraswati, E. Heraldi, M. A. Khafidhin, Y. K. Krisnandi, U. S. F. Arrozi and G. T. M. Kadja, *Chem. Pap.* **75**, 3253 (2021).
14. A. A. Azmi and M. A. A. Aziz, *J. Environ. Chem. Eng.* **7**, 103022 (2019).
15. M. K. Koh, Y. J. Wong, S. P. Chai and A. R. Mohamed, *J. Ind. Eng. Chem.* **62**, 156 (2018).
16. M. Perovic, Q. Qin and M. Oschatz, *Adv. Funct. Mater.* **30**, 1908371 (2020).
17. J. Wang, Y. Zhou and X. Hu, *Environ. Res.* **214**, 113855 (2022).
18. M. Wei, Q. Yu, T. Mu, L. Hou, Z. Zuo and J. Peng, *Adsorption* **22**, 385 (2016).
19. A. Popa, V. Sasca, O. Verdes, M. Suba and P. Barvinschi, *J. Therm. Anal. Calorim.* **134**, 269 (2018).
20. Á. Mastalir and Á. Molnár, *Coord. Chem. Rev.* **470**, 214696 (2022).
21. L. Zhang, Y. Li, H. Zhou and M. Chen, *Energy Fuels* **31**, 3062 (2017).
22. L. Zhang, Y. Li and H. Zhou, *Energy* **149**, 414 (2018).
23. F. Fernandes, F. Pinto, J. Villarroel-Rocha, K. Sapag, L. Souza, V. Caldeira and A. Santos, *Quím. Nova* **44**, 1117 (2021).
24. M. Ding, X. Liu, P. Ma and J. Yao, *Coord. Chem. Rev.* **465**, 214576 (2022).
25. J. A. A. Gibson, A. V. Gromov, S. Brandani and E. E. B. Campbell, *J. Porous Mater.* **24**, 1473 (2017).
26. F. Subhan, S. Aslam, Z. Yan and M. Yaseen, *Fuel Process. Technol.* **235**, 107351 (2022).
27. A. A. Dabbawala, *Microporous Mesoporous Mater.* **303**, 110261 (2020).
28. Z. Zhang, P. Li, T. Zhao and Y. Xia, *Adsorpt. Sci. Technol.* **2022**, 1 (2022).
29. A. Moya, M. Hernando-Pérez, M. Pérez-Illana, C. San Martín, J. Gómez-Herrero, J. Alemán, R.

- Mas-Ballesté and P. J. De Pablo, *Nanoscale* **12**, 1128 (2020).
30. R. Dawson, A. I. Cooper and D. J. Adams, *Polym. Int.* **62**, 345 (2013).
31. L. Ge, J. Wei, L. Geng, S. Chen and L. Liao, *J. Porous Mater.* **29**, 19 (2022).
32. Y. Jia, J. Wei, Y. Yuan, L. Geng, S. Chen and L. Liao, *J. Mater. Res.* **37**, 543 (2022).
33. Z. Lin, J. Wei, L. Geng, D. Mei and L. Liao, *Energy Technol.* **6**, 1618 (2018).
34. Y. Yuan, J. Wei, L. Geng, D. Mei and L. Liao, *RSC Adv.* **10**, 34187 (2020).
35. Y. Li, J. Wei, L. Geng, D. Mei and L. Liao, *Nano* **16**, 1 (2021).
36. M. Sari Yilmaz, *Microporous Mesoporous Mater.* **245**, 109 (2017).
37. M. Sari Yilmaz, *J. Porous Mater.* **30**, 1555 (2023).
38. M. Mirković, M. S. Yilmaz, L. Kljajević, V. Pavlović, M. Ivanović, D. Djukić and T. Eren, *Polymers* **15**, 1669 (2023).
39. A. L. Yaumi, *Energy* **124**, 121 (2017).
40. P. Zhao, G. Zhang, H. Yan and Y. Zhao, *Chin. J. Chem. Eng.* **35**, 17 (2021).
41. R. Chatterjee, B. Sajjadi, W.-Y. Chen, D. L. Mat-tern, N. O. Egiebor, N. Hammer and V. Raman, *Energy Fuels* **33**, 2366 (2019).
42. Z. Li, Z. Zhong, B. Zhang, W. Wang and W. Wu, *J. Anal. Appl. Pyrolysis* **138**, 103 (2019).
43. M. Popova, R. Mihaylova, G. Momekov, D. Momekova, H. Lazarova, I. Trendafilova, V. Mitova, N. Koseva, J. Mihályi, P. Shestakova, P. St. Petkov, H. A. Aleksandrov, G. N. Vayssilov, S. Konstantinov and Á. Szegedi, *Eur. J. Pharm. Biopharm.* **142**, 460 (2019).
44. Z. Lin, J. Wei, L. Geng, D. Mei and L. Liao, *RSC Adv.* **7**, 54422 (2017).
45. Z. Di, C. Yang, X. Jiao, J. Li, J. Wu and D. Zhang, *Fuel* **104**, 878 (2013).
46. Q. Li, W. Cong, C. Xu, S. Zhang, F. Wang, D. Han, G. Wang and L. Bing, *CrystEngComm* **23**, 8641 (2021).
47. T. Odedairo, R. J. Balasamy and S. Al-Khattaf, *J. Mol. Catal. A: Chem.* **345**, 21 (2011).
48. C. He, J. Li, P. Li, J. Cheng, Z. Hao and Z.-P. Xu, *Appl. Catal. B* **96**, 466 (2010).
49. T. Qi, J. Shi, X. Wang, K. Dong, Y. Luo, J. Teng, G.-W. Chu, H.-K. Zou and B. Sun, *Microporous Mesoporous Mater.* **311**, 110679 (2021).
50. J. Wang, M. Zhang, G. Li, Y. Zhou, Y. Zhang, W. Zhang, T. Jiao, Y. Zhang, P. Liang and H. Zhang, *Fuel* **286**, 119479 (2021).
51. Y. Xia and R. Mokaya, *J. Mater. Chem.* **14**, 863 (2004).
52. Y. Wang, T. Du, H. Jia, Z. Qiu and Y. Song, *Solid State Sci.* **97**, 105985 (2019).
53. H. Cheng, H. Song, S. Toan, B. Wang, K. A. M. Gasem, M. Fan and F. Cheng, *Chem. Eng. J.* **406**, 126882 (2021).
54. A. Goeppert, S. Meth, G. K. S. Prakash and G. A. Olah, *Energy Environ. Sci.* **3**, 1949 (2010).
55. F. Yin, L. Zhuang, X. Luo and S. Chen, *Appl. Surf. Sci.* **434**, 514 (2018).
56. N. Rao, M. Wang, Z. Shang, Y. Hou, G. Fan and J. Li, *Energy Fuels* **32**, 670 (2018).